



# Phosphorus migration mechanism between iron and high phosphorus gangue phase at high temperatures

Lei Guo<sup>1</sup> · Jin-tao Gao<sup>1</sup> · Sheng-ping Zhong<sup>1</sup> · Zhan-cheng Guo<sup>1</sup>

Received: 4 December 2017 / Revised: 11 March 2018 / Accepted: 13 March 2018 / Published online: 7 June 2018  
© China Iron and Steel Research Institute Group 2018

## Abstract

The phosphorus migration mechanism during melting separation of non-carbon-reduced high phosphorus iron ore was investigated. Firstly, the equilibrium compositions of hydrogen-reduced high phosphorus iron ore at different temperatures were simulated by the use of equilibrium composition module of HSC Chemistry software. Then, thermodynamic calculation was verified by the real heat treatment of simulated hydrogen-reduced high phosphorus iron ore with several pure reagents including self-made pure fluorapatite. The iron particles in the simulated samples gathered and grew up during heat treatment. Meanwhile, the hypoeutectic structure of Fe–P with grid shape of high phosphorus phase and circular shape of low phosphorus phase emerged within those iron particles. With the penetration of phosphorus from the periphery into the iron particles, the grid structure became denser and denser. It proves that the elemental phosphorus can be reduced from the gangue phase by metallic iron without solid carbon at high temperatures.

**Keywords** Melting separation · Fluorapatite · Thermodynamics · Phosphorus migration · High phosphorus iron ore

## 1 Introduction

The iron ore deposits have exhibited an increasingly complex mineralogical composition nowadays with the rapid consumption of iron ore resource around the world [1–3]. Statistically, the identified premium grade iron ore with phosphorus content lower than 0.05 wt% will be depleted within 30 years at the current rate of mining [4, 5]. Thus, we are compelled to exploit and utilize those worldwide high phosphorus iron ores. Nevertheless, the enrichment of phosphorus element in the metallic iron phase is always a big problem during thermometallurgy treatment of high phosphorus iron ore [6, 7]. It is of significant value for the development and utilization of high phosphorus iron ore to investigate the transformation and migration mechanism of phosphorus element [7]. There are various researches on dephosphorization of high phosphorus iron ore, including pyrometallurgy [7–13], hydrometallurgy [4, 14–19], biological metallurgy [20–23],

physical metallurgy [24–26] or their combinations [5, 27]. The phosphorus migration behavior in pyrometallurgy process was studied in this paper.

Phosphorus element mainly exists in the form of fluorapatite ( $\text{Ca}_5(\text{PO}_4)_3\text{F}$ ) in the high phosphorus iron ores of Hubei province, China [28]. For general coal-based reduction processes, the temperature is usually above 1473 K, under which condition the fluorapatite phase is easy to be reduced by solid carbon and generates gaseous phosphorus ( $\text{P}_2$ ), which is prone to be absorbed by carbon-bearing iron phase.

Irrespective of blast furnace process or rotary hearth furnace process, the main reducing agent is carbon; usually, the phosphorus element in the ore is considered to be reduced by carbon from fluorapatite to elemental phosphorus and then migrates into metallic iron phase. Fluorapatite cannot be reduced by gaseous reducing agents like CO or  $\text{H}_2$  according to thermodynamic principles. Solid carbon is not used in some direct reduction processes, e.g., shaft furnace [29] or fluidized bed [30, 31] processes. However, due to the adoption of CO containing reducing gas, the Boudouard reaction ( $2\text{CO}=\text{CO}_2 + \text{C}$ ) inevitably happens, resulting in a certain amount of carbon left in the direct-reduced iron (DRI) products and causing the

✉ Zhan-cheng Guo  
zcguo@ustb.edu.cn

<sup>1</sup> State Key Laboratory of Advanced Metallurgy, University of Science and Technology Beijing, Beijing 100083, China

reduction of fluorapatite in the subsequent processing. Of course, it can be speculated that using non-carbon gaseous reducing agents could avoid the generation of solid carbon and the reduction of fluorapatite phase in the subsequent processing. Then, the phosphorus element would be enriched in slag phase instead of metallic iron phase through melting separation process. However, in the hydrogen-fluidized reduction and melting separation experiment of high phosphorus iron ore, metallic iron obtained still contains large amounts of phosphorus although no carbonaceous reducing agent was used [32]. The phosphorus in the metallic iron is proved to exist in the form of phosphorus iron alloy. There are lots of researches on the phosphorus migration and distribution in coal-based reduction process of high phosphorus iron ore [6, 9, 33]. For example, Cheng et al. [6, 34] found that carburization of iron phase contributes to phosphorus enrichment, and phosphorus and carbon in iron phase present a consistent spatial distribution. However, for some gas-based direct reduction processes, there is just little or no carbon content in the product. Nevertheless, few literatures focus on the phosphorus migration mechanism during melting separation of reduced high phosphorus iron ore without carbon.

In this paper, the reaction and migration mechanism of phosphorus element in melting separation process of non-carbon reduced high phosphorus iron ore was studied. The aim is to sum up the characteristics and conditions of phosphorus enrichment in iron phase and to provide instructions and solutions for phosphorus removal of high phosphorus iron ore during gas-based direct reduction and melting separation process.

## 2 Experimental

### 2.1 Samples preparation and apparatus

Due to the complex nature of the oolitic structure, the phase interaction in the high phosphorus iron ore is complicated; it is difficult to clearly reveal the mechanism of direct reduction process of minerals or the migration of phosphorus during melting separation process when using the high phosphorus iron ore as raw material [35]. As a result, pure reagents were chosen as the raw materials to simulate the real iron ore in this study [6, 34]. In order to avoid the influence of other fluxes like alkaline oxides on the phosphorus migration, no flux was added during the melting separation treatment.

Firstly, the pure fluorapatite was prepared by  $\text{Ca}_3(\text{PO}_4)_2$  and  $\text{CaF}_2$ . These two reagents were mixed with the mole ratio of 3:1 and then compressed into briquettes and roasted at 1623 K for 1 h. After heat treatment, the samples shrunk and turned into light green color. To verify whether the

product was fluorapatite, the samples were crushed and milled into powder for X-ray diffraction (XRD) analysis. The XRD results are shown in Fig. 1. It is proved that the peak patterns of the self-made fluorapatite are very close to the standard fluorapatite XRD card, and all the peak widths are very small. Thus, the self-made fluorapatite is proved to be pure fluorapatite with high crystallization degree.

Table 1 shows the main components of high phosphorus iron ore used in experiments. The high phosphorus iron ore was reduced with 1 L/min Ar and 2 L/min  $\text{H}_2$  at 1073 K for 80 min in a fluidized bed. The final metallization ratio is about 70%, and the content of metallic iron should be  $67.28\% \times (112/160) \times 70\% = 32.97\%$ . The unreduced iron oxide  $\text{Fe}_x\text{O}$  may exist in the form of fayalite ( $\text{Fe}_2\text{SiO}_4$ ) or hercynite ( $\text{FeAl}_2\text{O}_4$ ). The weight percentage of other components like  $\text{SiO}_2$  or  $\text{Al}_2\text{O}_3$  increases about 19% after reduction due to the oxygen loss.

Hydrogen-reduced high phosphorus iron ore was simulated with several pure reagents like calcium oxide, silicon dioxide, aluminum oxide, iron powder and self-made pure fluorapatite. All these reagents are of analytic grade. The particle size of iron powder is about 180  $\mu\text{m}$ , and other reagents are below 75  $\mu\text{m}$ . These substances were weighed according to the contents in Table 1 except for iron powder. The content of metallic iron in the mixture was decreased to 10% for the convenience of phosphorus migration investigation. Then, all these substances except for iron powder were mixed and ground to simulate the interaction conditions in the real high phosphorus iron ore. Then, all the reagents were compressed into columnar briquettes with the diameter of 10 mm and mass of 1.0 g. The briquetting pressure was about 300 MPa. The iron powders were evenly distributed in the briquettes, surrounded by gangue phases as shown in Fig. 2.

To simulate the real melting separation process of direct-reduced high phosphorus iron ore, those briquettes were heat-treated in a horizontal tube furnace as illustrated in Fig. 2. Rapid heating operation was conducted to reduce

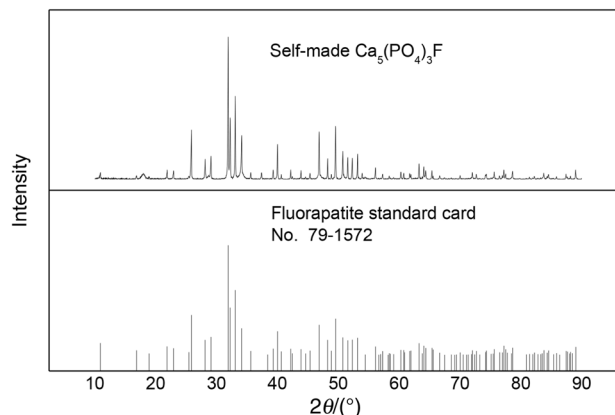


Fig. 1 XRD result of self-made fluorapatite

**Table 1** Main components of high phosphorus iron ore (wt%)

Ca <sub>5</sub> (PO <sub>4</sub> ) <sub>3</sub> F	SiO <sub>2</sub>	Al <sub>2</sub> O <sub>3</sub>	CaO	Fe <sub>2</sub> O <sub>3</sub>
5.47	13.71	6.8	1.01	67.28

the effect of temperature-rising period. Meanwhile, rapid cooling operation was used to remain the original state of the samples. Firstly, the briquettes were put into alumina crucibles with an inner diameter of 12 mm. When the tube furnace rose to the target temperature, the alumina crucibles together with the briquettes were moved to the constant temperature zone. A low-density refractory brick was used to segregate the cold crucible and the hot furnace tube. During the experiments, the argon gas as shielding gas was kept passing through the furnace tube. After heat treatment, the samples were taken out and cooled in argon gas atmosphere. Then, the samples were inlaid in resin and polished. As shown in Fig. 3, except for some individual Al<sub>2</sub>O<sub>3</sub> and SiO<sub>2</sub> particles, Al, Si and Ca elements are evenly distributed in the sample after heat treatment.

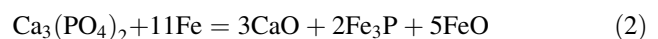
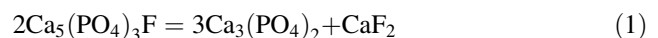
Relative analytical instruments utilized in this study are X-ray diffractometer [SmartLab(9)] and scanning electron microscope with energy-dispersive spectrometer (Bruker Nano GmbH CrystAlign 400).

## 2.2 Thermodynamic analysis of non-carbon fluorapatite reduction

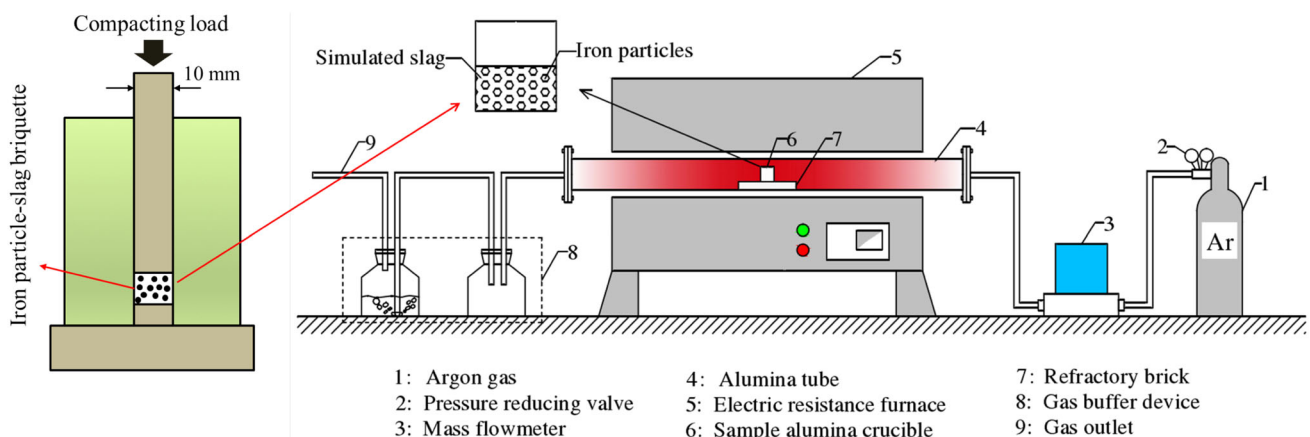
The equilibrium compositions of hydrogen-reduced high phosphorus iron ore were simulated by the use of equilibrium composition module of HSC Chemistry software. The input composition parameters as listed in Table 2 were defined according to the hydrogen-reduced high phosphorus iron ore. Neither carbon monoxide nor other solid carbon was used in the reduction process; thus, there was no carbon in the post-reduced iron ore.

The starting material was considered to be 1000 kg, and the mole numbers of every substance were Ca<sub>5</sub>(PO<sub>4</sub>)<sub>3</sub>F 0.108 kmol, SiO<sub>2</sub> 2.28 kmol, Al<sub>2</sub>O<sub>3</sub> 0.667 kmol, CaO 0.180 kmol and Fe 5.89 kmol. Other phases possibly generated at high temperature were preset in the software, and they were P<sub>2</sub> (g), CaF<sub>2</sub>, CaO·Al<sub>2</sub>O<sub>3</sub>, CaO·2Al<sub>2</sub>O<sub>3</sub>, CaO·Al<sub>2</sub>O<sub>3</sub>·SiO<sub>2</sub>, CaAl<sub>2</sub>Si<sub>2</sub>O<sub>8</sub>, CaO·Al<sub>2</sub>O<sub>3</sub>·2SiO<sub>2</sub>, Ca<sub>3</sub>(PO<sub>4</sub>)<sub>2</sub>, CaSiO<sub>3</sub>, FeAl<sub>2</sub>O<sub>4</sub>, FeO, Fe<sub>2</sub>SiO<sub>4</sub>, FeP, FeP<sub>2</sub>, Fe<sub>2</sub>P and Fe<sub>3</sub>P. The nitrogen gas atmosphere was introduced. The equilibrium amounts of different phases at different temperatures are shown in Fig. 4a–e.

Theoretically, the amounts of CaO·Al<sub>2</sub>O<sub>3</sub>, CaO, Fe<sub>2</sub>P, FeP and CaO·2Al<sub>2</sub>O<sub>3</sub> are no more than 0.0025 kmol in the reaction system below 1073 K, and their equilibrium amounts increase to different levels with the temperature increasing. The equilibrium amount of Ca<sub>3</sub>(PO<sub>4</sub>)<sub>2</sub> shows a small peak at 773 K while nearly disappears at other temperatures. Figure 4b shows that Ca<sub>5</sub>(PO<sub>4</sub>)<sub>3</sub>F disappears above 873 K, and simultaneously, Ca<sub>3</sub>(PO<sub>4</sub>)<sub>2</sub> is unstable in this system as indicated above; thus, the phosphorus element is easy to combine with Fe in the form of Fe<sub>3</sub>P as shown in Fig. 4c. The only reducing agent in this system is Fe and its oxidation product is FeO. Part of FeO transforms into phases like FeAl<sub>2</sub>O<sub>4</sub> and Fe<sub>2</sub>SiO<sub>4</sub>, and FeAl<sub>2</sub>O<sub>4</sub> is dominant as shown in Fig. 4b, d. Most of CaO and Al<sub>2</sub>O<sub>3</sub> stay in the form of CaO·Al<sub>2</sub>O<sub>3</sub>, CaO·Al<sub>2</sub>O<sub>3</sub>·SiO<sub>2</sub>, CaAl<sub>2</sub>Si<sub>2</sub>O<sub>8</sub>, CaO·Al<sub>2</sub>O<sub>3</sub>·2SiO<sub>2</sub> and CaSiO<sub>3</sub>, while about a half of SiO<sub>2</sub> does not change its state due to its high original amount. According to the simulated results, the reduction process of Ca<sub>5</sub>(PO<sub>4</sub>)<sub>3</sub>F should be:



The formation of phases like FeAl<sub>2</sub>O<sub>4</sub>, Fe<sub>2</sub>SiO<sub>4</sub>, CaO·Al<sub>2</sub>O<sub>3</sub>, CaO·Al<sub>2</sub>O<sub>3</sub>·SiO<sub>2</sub>, CaAl<sub>2</sub>Si<sub>2</sub>O<sub>8</sub>, CaO·Al<sub>2</sub>O<sub>3</sub>·2SiO<sub>2</sub> and CaSiO<sub>3</sub> contributes to the decrease in Gibbs free energy of Eq. (2) and promotes this reaction.

**Fig. 2** Experimental setup of the heat treatment experiment

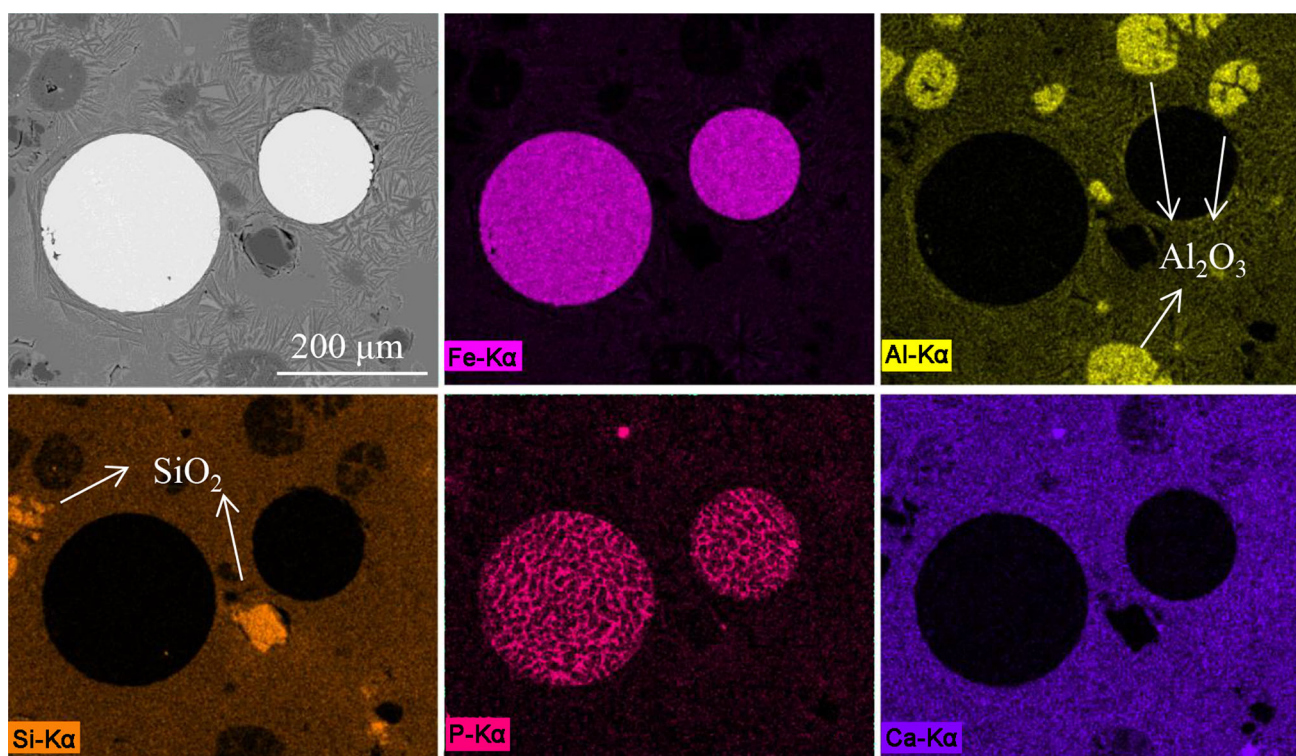


**Fig. 3** Sectional element distribution after heat treatment for 10 min at 1673 K

**Table 2** Main components of hydrogen-reduced high phosphorus iron ore (wt%)

$\text{Ca}_5(\text{PO}_4)_3\text{F}$	$\text{SiO}_2$	$\text{Al}_2\text{O}_3$	$\text{CaO}$	$\text{Fe}$	Unreacted $\text{Fe}_x\text{O}$
6.51	16.31	8.1	1.2	39.23	Balance

The specific equilibrium amounts of different phases at three typical temperatures are listed in Table 3. The equilibrium amounts of  $\text{FeP}_2$  and  $\text{P}_2$  (g) are always below  $10^{-8}$  and  $10^{-10}$  kmol (the last two lines in Table 3); thus, they are not illustrated in Fig. 4. The low equilibrium amount of  $\text{P}_2$  (g) proves that it is not stable in this system and very easy to be absorbed by Fe phase. Meanwhile, part of  $\text{P}_2$  (g) may also volatilize into gas phase in practice.

It should be pointed out that all these simulated results were obtained only considering the thermodynamic feasibilities and ignoring the kinetic limitations. The simulated equilibrium compositions are difficult to be obtained at relatively low temperatures owing to kinetic limitations. Consequently, those simulated equilibrium compositions are of reference values at high temperatures only.

### 2.3 Melting separation experiment under no carbon condition

Before experiment, the melting point of the sample briquettes was tested with an in situ melting point analyzer. The

samples were firstly compressed into cylindrical briquettes of  $\phi 6 \text{ mm} \times 6 \text{ mm}$ . Then, the briquettes were heated from room temperature at the heating rate of 10 K/min and the melting process is shown in Fig. 5. It is shown that the briquettes started to shrink and soften from 1631 K, and the briquettes completely melt 2 min later after the temperature reached 1651 K. According to the melting property of the briquettes, the temperature of following heat treatment experiments was chosen above 1623 K.

The procedures of the heat treatment have been described in Sect. 2.1. Three heat treatment temperatures (1623, 1673, 1723 K) and four holding time (5, 10, 15, 20 min) were determined before experiment. Those sample numbers under different heat treatment conditions are listed in Table 4.

## 3 Results and discussion

### 3.1 Morphology of post-experiment samples

After heat treatment, the samples were inlaid in resin and polished as shown in Fig. 6. For samples a, b, c and e, due to the relatively low heating temperature and short holding time, the slag phase of them was not well sintered; as a consequence, the iron particles fell off from the briquettes during polishing treatment. Thus, the cross section of iron



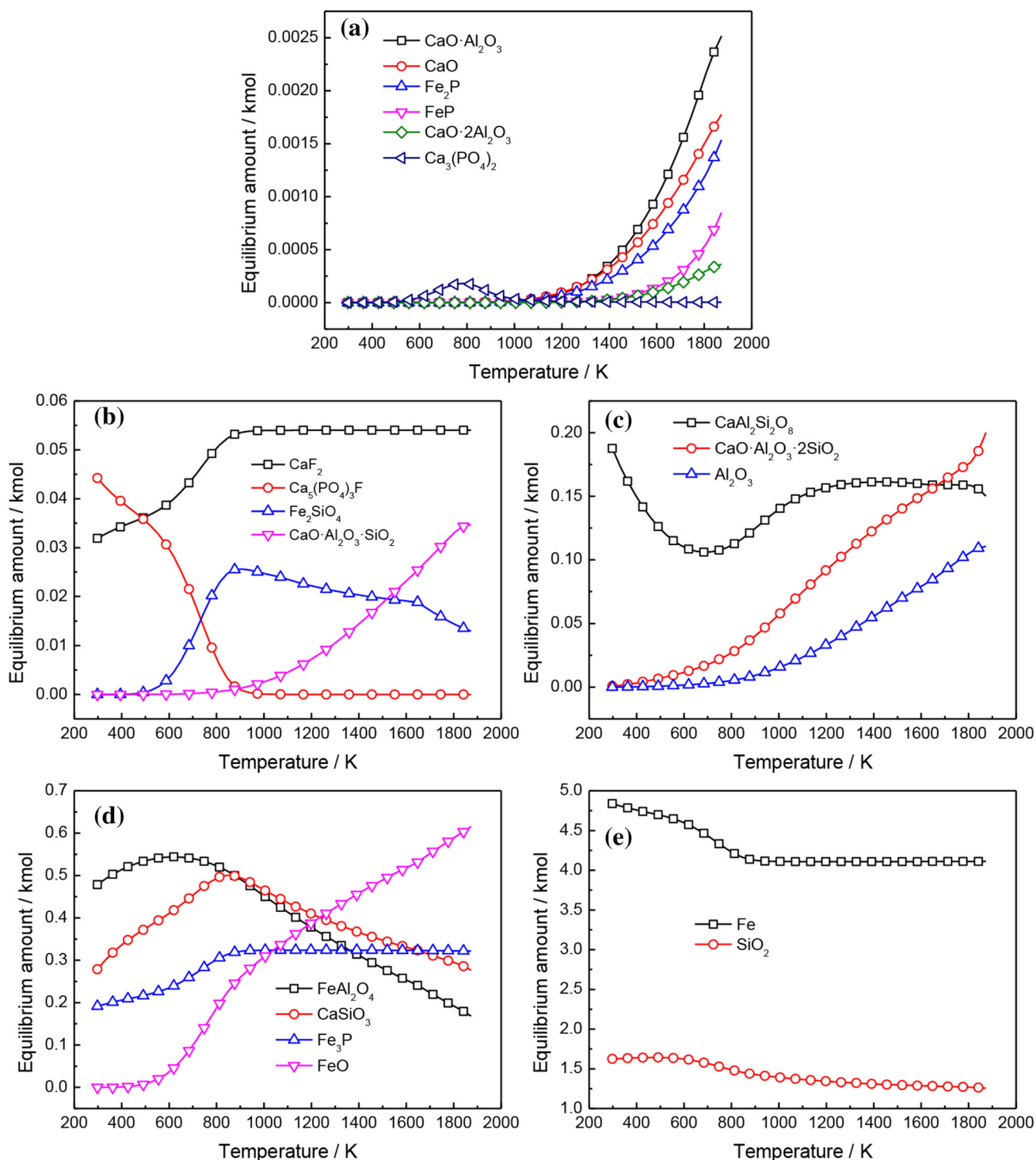


Fig. 4 Equilibrium amounts of different phases at different temperatures

particles in samples a, b, c and e was not able to be obtained. The slag phase of these four samples shows white color, while the slag phase of others well sintered shows green color.

As shown in Fig. 6, the melting effect of slag phase becomes better with the increases in temperature and

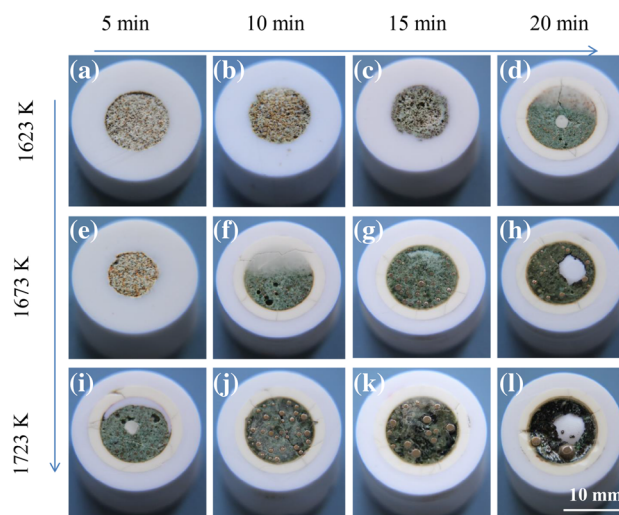
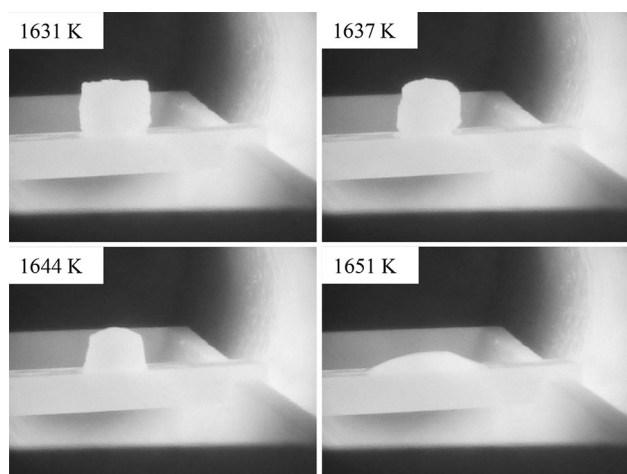
holding time, which is also reflected in the color of slag phase. The color changing sequence is white, light green and dark green. Meanwhile, the particle size of metallic iron increases with better melting conditions as illustrated by the cross section of briquettes, which indicates that those small iron particles mixed in the original material

**Table 3** Equilibrium amounts of different phases at three temperatures (kmol)

Phase	Temperature/K		
	1623	1673	1723
Fe	4.11	4.11	4.11
SiO <sub>2</sub>	1.28	1.28	1.28
FeO	0.525	0.540	0.560
CaSiO <sub>3</sub>	0.327	0.319	0.309
Fe <sub>3</sub> P	0.323	0.323	0.323
FeAl <sub>2</sub> O <sub>4</sub>	0.247	0.234	0.217
CaO·Al <sub>2</sub> O <sub>3</sub> ·2SiO <sub>2</sub>	0.153	0.159	0.166
CaAl <sub>2</sub> Si <sub>2</sub> O <sub>8</sub>	0.159	0.159	0.159
N <sub>2</sub> (g)	0.100	0.100	0.100
Al <sub>2</sub> O <sub>3</sub>	$8.17 \times 10^{-2}$	$8.72 \times 10^{-2}$	$9.42 \times 10^{-2}$
CaF <sub>2</sub>	$5.40 \times 10^{-2}$	$5.40 \times 10^{-2}$	$5.40 \times 10^{-2}$
CaO·Al <sub>2</sub> O <sub>3</sub> ·SiO <sub>2</sub>	$2.42 \times 10^{-2}$	$2.64 \times 10^{-2}$	$2.89 \times 10^{-2}$
Fe <sub>2</sub> SiO <sub>4</sub>	$1.90 \times 10^{-2}$	$1.82 \times 10^{-2}$	$1.66 \times 10^{-2}$
CaO·Al <sub>2</sub> O <sub>3</sub>	$1.10 \times 10^{-3}$	$1.32 \times 10^{-3}$	$1.60 \times 10^{-3}$
CaO	$8.59 \times 10^{-4}$	$1.01 \times 10^{-3}$	$1.18 \times 10^{-3}$
Fe <sub>2</sub> P	$6.26 \times 10^{-4}$	$7.46 \times 10^{-4}$	$8.98 \times 10^{-4}$
FeP	$1.73 \times 10^{-4}$	$2.33 \times 10^{-4}$	$3.23 \times 10^{-4}$
CaO·2Al <sub>2</sub> O <sub>3</sub>	$1.21 \times 10^{-4}$	$1.54 \times 10^{-4}$	$2.00 \times 10^{-4}$
Ca <sub>3</sub> (PO <sub>4</sub> ) <sub>2</sub>	$5.19 \times 10^{-6}$	$4.55 \times 10^{-6}$	$3.52 \times 10^{-6}$
Ca <sub>5</sub> (PO <sub>4</sub> ) <sub>3</sub> F	$1.11 \times 10^{-7}$	$6.91 \times 10^{-8}$	$3.42 \times 10^{-8}$
FeP <sub>2</sub>	$1.18 \times 10^{-9}$	$2.38 \times 10^{-9}$	$5.06 \times 10^{-9}$
P <sub>2</sub> (g)	$1.10 \times 10^{-12}$	$4.02 \times 10^{-12}$	$1.59 \times 10^{-11}$

**Table 4** Sample number under different heat treatment conditions

Temperature/K	Sample number at different holding time			
	5 min	10 min	15 min	20 min
1623	a	b	c	d
1673	e	f	g	h
1723	i	j	k	l

**Fig. 6** Cross section morphology of briquettes after heat treatment**Fig. 5** In situ observation of briquette melting behavior

will gradually gather and “grow up” during heat treatment. The diameter of original iron particles is about 178  $\mu\text{m}$ , while it even grows to 3 mm in sample 1.

In a previous experiment, the mass of briquettes was 0.6 g with diameter of 6 mm and heating temperature of

1653 K. The briquettes were well sintered just with 5 min of holding time as shown in Fig. 7. That is owing to the smaller size of briquette and the use of wide-mouthed crucibles, which provide better heat transfer conditions between the furnace and briquettes. Differently, the briquettes were water-quenched immediately after heat treatment in this experiment; thus, the original melting state of those samples was better kept compared with those quenched with argon gas.

Figure 7 shows that the porous and irregular morphology of original iron particles was remained in the sample with holding time of 5 min. The pores in the iron particles disappeared gradually with the increase in holding time, but the irregular shape was remained (10 min). Finally, the iron particles changed into regular spheres with the effect of surface tension (15 and 20 min).

In this experiment, all the involved iron particles in the briquettes after heat treatment showed spherical shape and no intermediate state was found. It can be inferred that, owing to the long period of cooling, those iron particles in gathering state and in irregular shape have enough time to change into spherical shape.

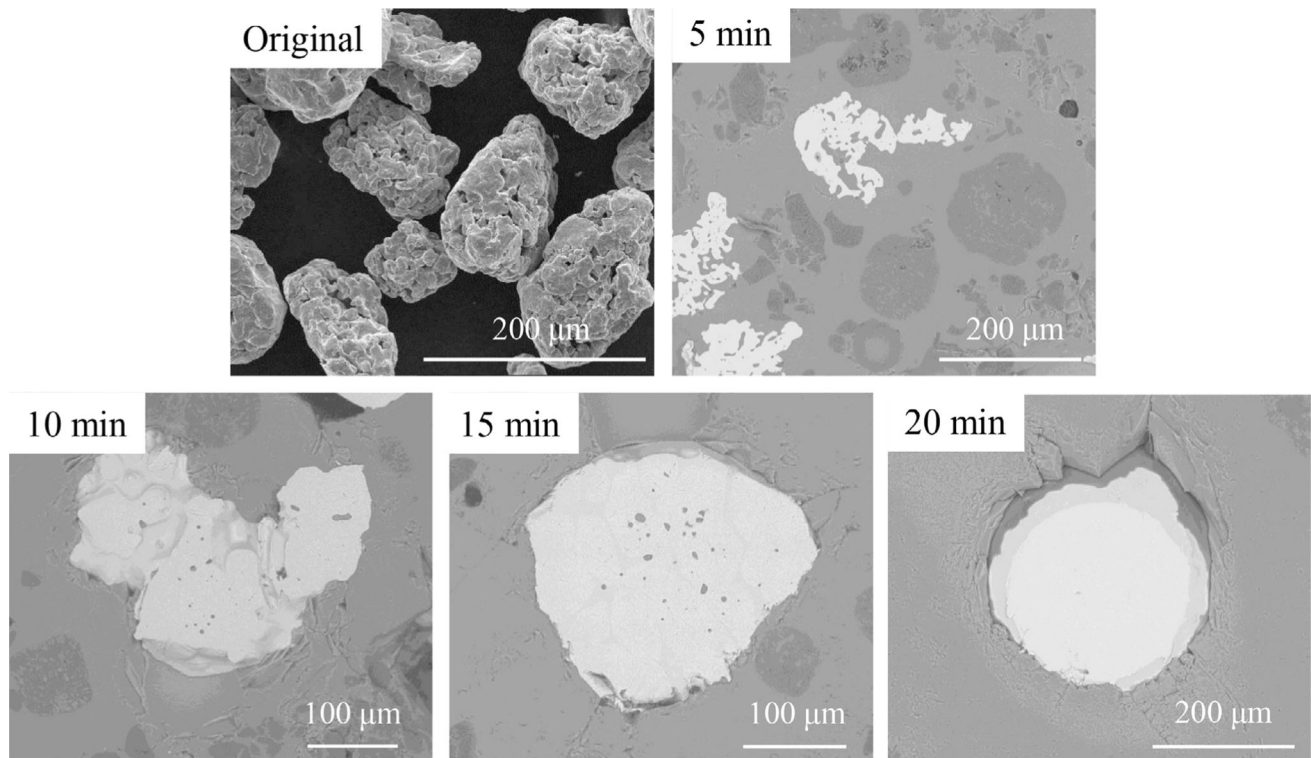


Fig. 7 Morphology evolution of iron particles during heat treatment (1653 K, water-quenched)

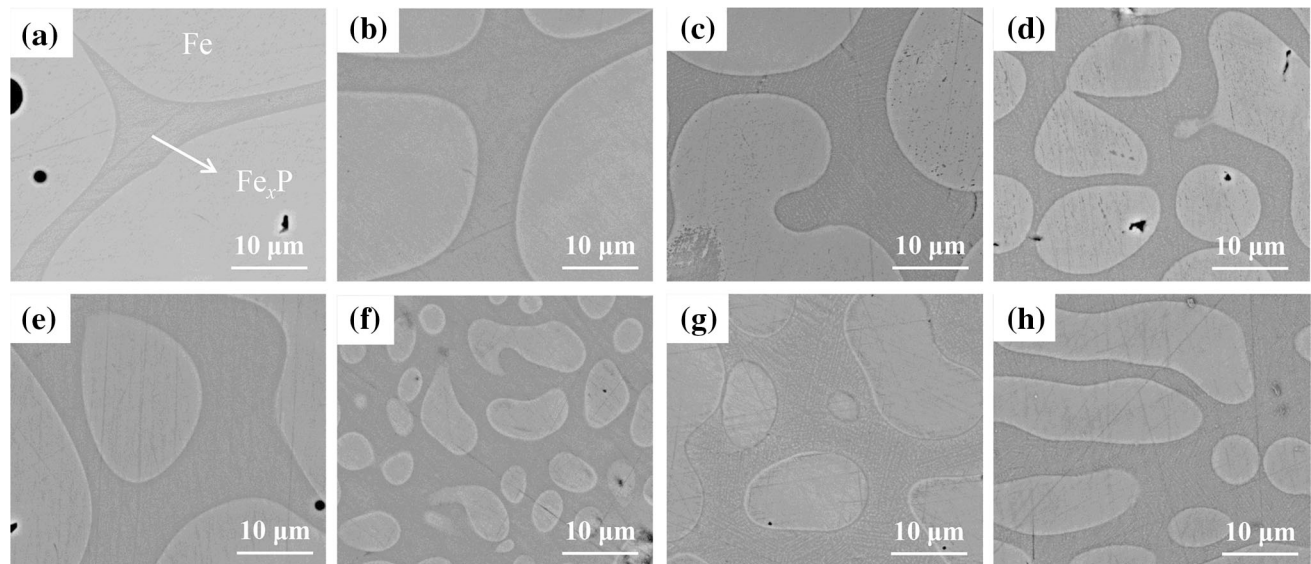


Fig. 8 Cross section morphology of iron particles after grinding under backscattered scanning electron microscope. **a** Sample d; **b** sample f; **c** sample g; **d** sample h; **e** sample i; **f** sample j; **g** sample k; **h** sample l

### 3.2 Cross section morphology of iron particles

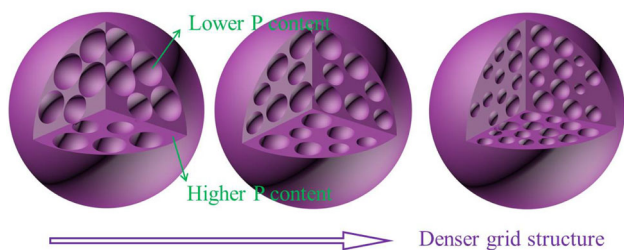
Figure 8 shows the backscattered scanning electron microscope images of samples d and f-l under the same magnification. According to the result of energy dispersive spectroscopy (EDS) analysis, the grid shape area (GSA) is

the  $\text{Fe}_x\text{P}$  phase with higher phosphorus content, and the circular shape area (CSA) is the iron phase with lower phosphorus content. It can be seen that the GSA becomes denser with the increase in heating temperature and holding time. Figure 9 shows the schematic three-dimensional structure within the iron particles.



### 3.3 Phosphorus distribution characteristics in metallic iron

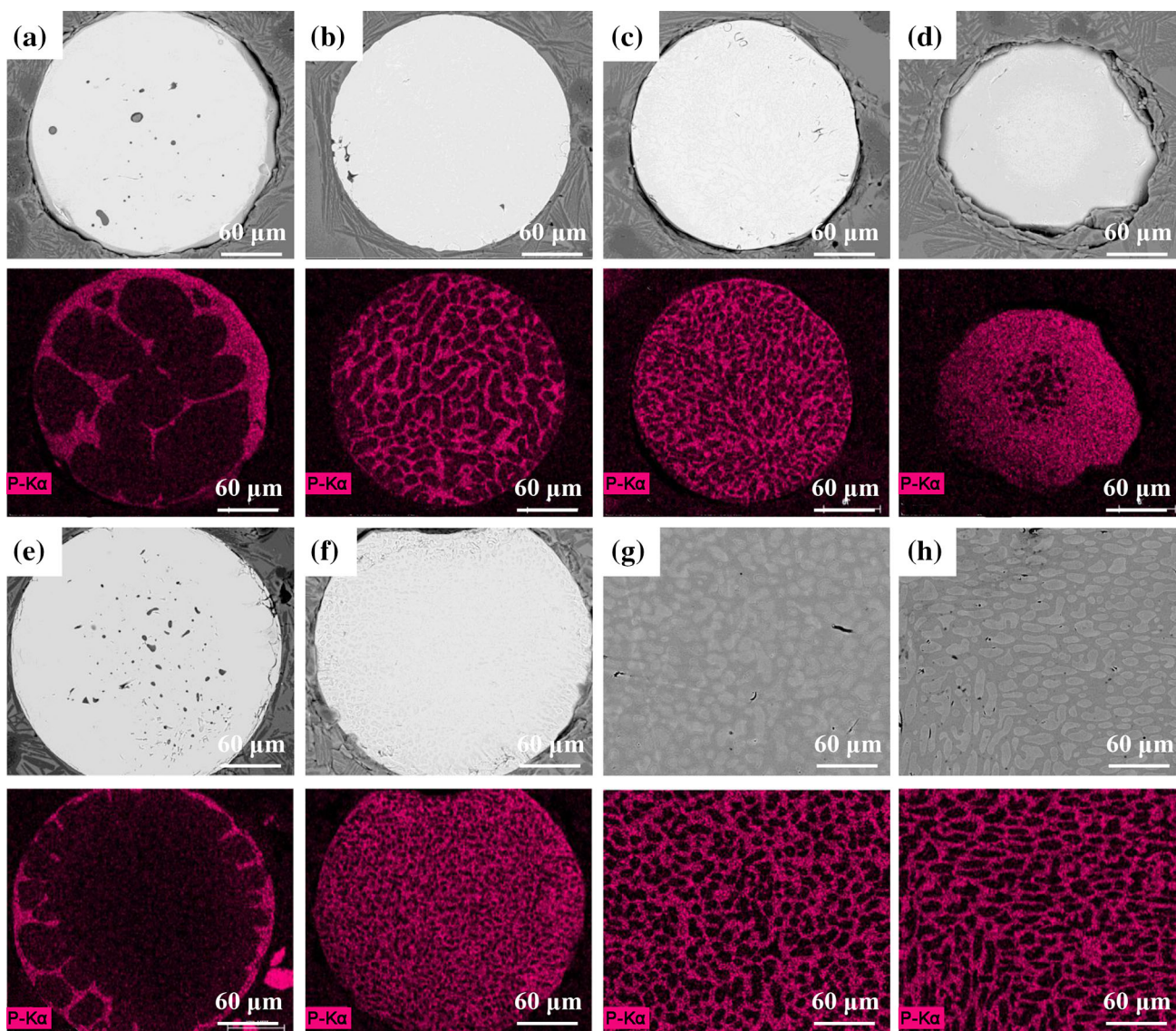
Figure 10 shows the cross-sectional EDS mapping images of phosphorus in iron particles at the same magnification scale.



**Fig. 9** Schematic diagram of phosphorus migration evolution process in metallic iron particles

The iron particles in samples k and l are larger than those in other samples; thus, their mapping images just show local area of the whole particle. As shown in Fig. 10a, e, the migration of phosphorus element starts from the periphery of iron particles and gradually develops toward the inner part to form grid structure. Generally, the grid density increases with the increase in heating temperature and holding time.

Compositions of the GSA and the CSA in every sample were determined with the EDS analysis method, and the data are listed in Table 5. Typically, regardless of the change in experimental conditions, the compositions in these two kinds of areas are nearly constant. Theoretically, there is no carbon element in the samples; the carbon content listed in Table 5 was contaminated by the diamond paste during polishing. The contents of Fe and P besides carbon were recalculated and are listed in Table 5. Without carbon, the mean contents

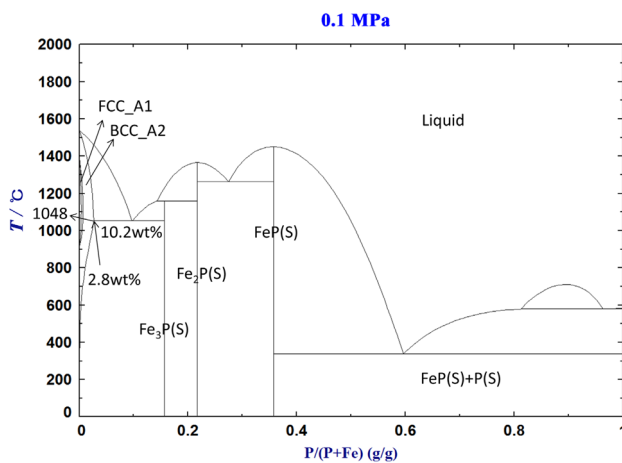


**Fig. 10** EDS mapping images of phosphorus. **a** Sample d; **b** sample f; **c** sample g; **d** sample h; **e** sample i; **f** sample j; **g** sample k; **h** sample l



**Table 5** Compositions of GSA and CSA in each sample (wt%)

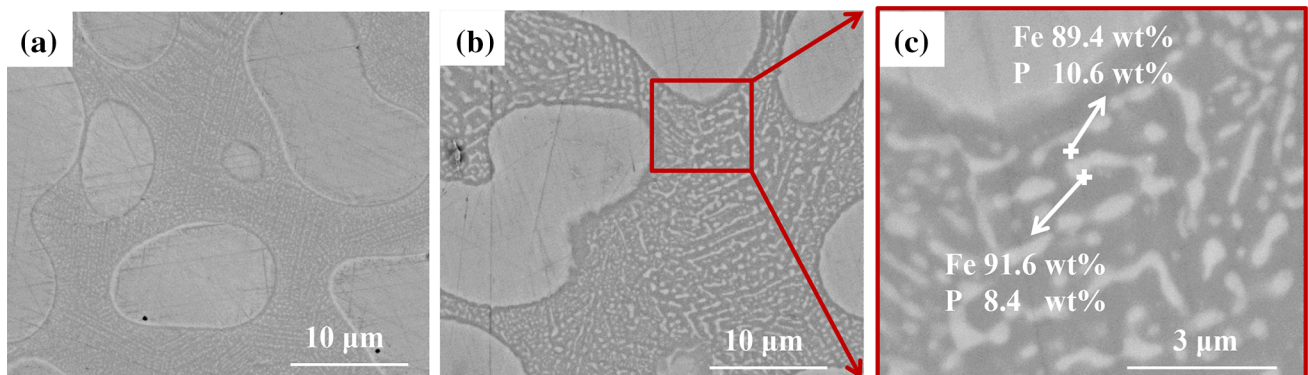
Sample no.	Area	Carbon content	Fe content		P content	
			C included	C excluded	C included	C excluded
d	GSA	20.3	69.2	86.8	10.5	13.2
	CSA	18.8	78.7	96.9	2.5	3.1
f	GSA	22.6	67.6	87.3	9.8	12.7
	CSA	19.3	78.1	96.8	2.6	3.2
g	GSA	19.6	69.8	86.8	10.6	13.2
	CSA	15.0	82.2	96.7	2.8	3.3
h	GSA	6.2	81.9	87.3	11.9	12.7
	CSA	4.3	92.5	96.6	3.2	3.4
i	GSA	5.5	81.9	86.7	12.6	13.3
	CSA	4.2	92.6	96.6	3.2	3.4
j	GSA	5.9	82.8	87.9	11.3	12.1
	CSA	4.5	92.1	96.4	3.4	3.6
k	GSA	5.9	82.3	87.5	11.8	12.5
	CSA	4.2	92.9	96.9	2.9	3.1
l	GSA	5.0	84.7	89.1	10.3	10.9
	CSA	4.5	93.1	97.5	2.4	2.5

**Fig. 11** Binary phase diagram of Fe–P

of Fe and P in the GSA among those samples are 87.4 and 12.6 wt%, and in the CSA, the data are 96.8 and 3.2 wt%, respectively. The element molar ratio between Fe and P in the GSA is about 3.8, and in the CSA, it is 16.7.

## 4 Discussion

According to the EDS analysis, the phosphorus contents in the GSA and CSA are in accordance with the hypoeutectic phase as illustrated in the Fe–P binary phase diagram in Fig. 11. Therefore, it can be inferred that the grid shape structure displayed in Figs. 8 and 10 are typical hypoeutectic structure of Fe–P alloy. And the detailed structure of GSA shown in Fig. 12 is the typical eutectic structure.

**Fig. 12** Detailed structure in GSA. **a** Sample k; **b** sample l; **c** partially enlarged view of **b**

Cheng et al. [6] thought that the absorption of phosphorus by iron is connected with the carburization process, and the reason of grid shape distribution of phosphorus is the non-uniform melting of metallic iron. According to the experimental phenomenon under no carbon conditions, the authors think that the influence of Fe–P binary alloy structure on the formation of grid shape structure in the iron phase should be emphasized.

It is concluded in this study that phosphorus element in non-carbon reduced high phosphorus iron ore can be reduced and absorbed by metallic iron phase during melting separation at high temperatures. This is not beneficial to process high phosphorus iron ore through reduction and melting separation process. Because it is very hard to prevent phosphorus from alloying with metallic iron phase compared to preventing the reduction of  $\text{Ca}_5(\text{PO}_4)_3\text{F}$  phase, the key point to avoid or reduce the aggregation of phosphorus in metallic iron phase is to avoid the reduction of  $\text{Ca}_5(\text{PO}_4)_3\text{F}$  by solid carbon or metallic iron during melting separation. Accordingly, decreasing the melting separation temperature and accelerating the slag/iron separation process can be effective [36].

## 5 Conclusions

According to the results of thermodynamic analysis of non-carbon fluorapatite reduction in the hydrogen-reduced high phosphorus iron ore, theoretically,  $\text{Ca}_5(\text{PO}_4)_3\text{F}$  disappears above 873 K, and  $\text{Ca}_3(\text{PO}_4)_2$  is unstable and easy to be reduced by Fe in this system. The phosphorus element is easy to be absorbed by metallic iron phase.

The iron particles in the simulated hydrogen-reduced high phosphorus iron ore gathered into larger spherical ones after heat treatment. According to the EDS analysis, the grid shape phase with higher phosphorus and circular shape iron phase with lower phosphorus in the iron particles are in accordance with the structure of hypoeutectic phase of Fe–P alloy.

The migration of phosphorus element starts from the periphery of iron particles and gradually develops toward the inner part to form grid structure. Generally, the grid density increases with the increase in heating temperature and holding time.

**Acknowledgements** This study is supported by the China Postdoctoral Science Foundation (2017M610768), the Open Projects of State Key Laboratory of Advanced Metallurgy (No. 41617013) and the National Key Research and Development Plan of China (2016YFB0601304).

## References

[1] A.R. Firth, J.F. Garden, *Metall. Mater. Trans. B* 39 (2008) 524–533.

- [2] K. Meijer, C. Zeilstra, C. Teerhuis, M. Ouwehand, J. van der Stel, *Trans. Indian Inst. Met.* 66 (2013) 475–481.
- [3] A. Hasanbeigi, M. Arens, L. Price, *Renew. Sustain. Energ. Rev.* 33 (2014) 645–658.
- [4] C.Y. Cheng, V.N. Misra, J. Clough, R. Muni, *Miner. Eng.* 12 (1999) 1083–1092.
- [5] H. Han, D. Duan, P. Yuan, S. Chen, *Ironmak. Steelmak.* 42 (2015) 542–547.
- [6] C. Cheng, Q.G. Xue, G. Wang, Y.Y. Zhang, J.S. Wang, *Metall. Mater. Trans. B* 47 (2016) 154–163.
- [7] H.Q. Tang, Y.Q. Qin, T.F. Qi, *Miner. Process. Extr. Metall. Rev.* 37 (2016) 236–245.
- [8] S.J. Bai, S.M. Wen, D.W. Liu, W.B. Zhang, Y.J. Xian, *ISIJ Int.* 51 (2011) 1601–1607.
- [9] Y.L. Li, T.C. Sun, A.H. Zou, C.Y. Xu, *Int. J. Min. Sci. Technol.* 22 (2012) 323–328.
- [10] R. Inoue, H. Suito, *ISIJ Int.* 46 (2006) 188–194.
- [11] C.Y. Xu, T.C. Sun, J. Kou, Y.L. Li, X.L. Mo, L.G. Tang, *Trans. Nonferrous Met. Soc. China* 22 (2012) 2806–2812.
- [12] H.Q. Tang, Z.C. Guo, Z.L. Zhao, *J. Iron Steel Res. Int.* 17 (2010) No. 9, 1–6.
- [13] W. Yu, T.C. Sun, J. Kou, Y.X. Wei, C.Y. Xu, Z.Z. Liu, *ISIJ Int.* 53 (2013) 427–433.
- [14] J.T. Yu, Z.C. Guo, H.Q. Tang, *ISIJ Int.* 53 (2013) 2056–2064.
- [15] M.J. Fisher-White, R.R. Lovel, G.J. Sparrow, *ISIJ Int.* 52 (2012) 1794–1800.
- [16] T.R.C. Patrick, R.R. Lovel, *ISIJ Int.* 41 (2001) 128–135.
- [17] M.J. Fisher-White, R.R. Lovel, G.J. Sparrow, *ISIJ Int.* 52 (2012) 797–803.
- [18] W.T. Xia, Z.D. Ren, Y.F. Gao, *J. Iron Steel Res. Int.* 18 (2011) No. 5, 1–4.
- [19] Y.S. Jin, T. Jiang, Y.B. Yang, Q. Li, G.H. Li, Y.F. Guo, *J. Cent. South Univ. Technol.* 13 (2006) 673–677.
- [20] T.M. Bhatti, W. Yawar, *Hydrometallurgy* 103 (2010) 54–59.
- [21] O. Priha, T. Sarlin, P. Blomberg, L. Wendling, J. Mäkinen, M. Arnold, P. Kinnunen, *Hydrometallurgy* 150 (2014) 269–275.
- [22] P. Delvasto, A. Valverde, A. Ballester, J.A. Muñoz, F. González, M.L. Blázquez, J.M. Igual, C. García-Balboa, *Hydrometallurgy* 92 (2008) 124–129.
- [23] P. Delvasto, A. Ballester, J.A. Muñoz, F. González, M.L. Blázquez, J.M. Igual, A. Valverde, C. García-Balboa, *Miner. Eng.* 22 (2009) 1–9.
- [24] K. Ionkov, S. Gaydardzhiev, A. Correa de Araujo, D. Bastin, M. Lacoste, *Miner. Eng.* 46–47 (2013) 119–127.
- [25] E. Matinde, M. Hino, *ISIJ Int.* 51 (2011) 544–551.
- [26] E. Matinde, M. Hino, *ISIJ Int.* 51 (2011) 220–227.
- [27] M. Omran, T. Fabritius, R. Mattila, *Powder Technol.* 269 (2015) 7–14.
- [28] D.Q. Zhu, T.J. Chun, J. Pan, L.M. Lu, Z. He, *Int. J. Miner. Metall. Mater.* 20 (2013) 505–513.
- [29] T. Harada, H. Tanaka, *ISIJ Int.* 51 (2011) 1301–1307.
- [30] L. Guo, Z.R. Yang, J.T. Gao, Y.W. Zhong, Z.C. Guo, *ISIJ Int.* 56 (2016) 736–743.
- [31] B. Weiss, J. Sturn, S. Voglsam, F. Winter, J. Schenk, *Chem. Eng. Sci.* 66 (2011) 703–708.
- [32] L. Guo, J.T. Gao, Y.W. Zhong, H. Gao, Z.C. Guo, *ISIJ Int.* 55 (2015) 1806–1815.
- [33] Y.S. Sun, Y.L. Han, P. Gao, Y.J. Li, *ISIJ Int.* 56 (2016) 1697–1704.
- [34] C. Cheng, Q.G. Xue, Y.Y. Zhang, F. Han, J.S. Wang, *ISIJ Int.* 55 (2015) 2576–2581.
- [35] H. Gao, L. Guo, J.T. Gao, Z.C. Guo, *Chin. J. Eng.* 37 (2015) 1284–1290.
- [36] J.T. Gao, L. Guo, Y.W. Zhong, H.R. Ren, Z.C. Guo, *Int. J. Miner. Metall. Mater.* 23 (2016) 743–750.